Electromagnetic Vibration Characteristics Analysis of a Squirrel-Cage Induction Motor Under Different Loading Conditions

DEFENG KONG, ZHIJUN SHUAI, WANYOU LI, AND DONGHUA WANG

College of Power and Energy Engineering, Harbin Engineering University, Harbin 150001, China

Corresponding author: Zhijun Shuai (shuaizhijun@hrbeu.edu.cn)

ABSTRACT Electromagnetic vibration is an important excitation source for squirrel-cage induction motors. However, the electromagnetic vibration under various loadings has not been sufficiently analyzed. It is proposed in this paper that the electromagnetic vibration of motors under different loads can be obtained by analyzing the amplitude of the electromagnetic force wave. The Maxwell tensor method is employed to derive the spatial and temporal distributions of the radial force. This paper also calculates the radial force using the finite element method and decodes the calculated results using two dimensional fast Fourier transform (2D-FFT) to determine the amplitude of the electromagnetic force at the spatial order under different loads. In addition, through the modal analysis of the stator core, it can be concluded that in the case of nonresonance, the vibration response increases when the electromagnetic force of the first-order and second-order rotor slot harmonic increases. Finally, the conclusion is verified by separating the electromagnetic vibration of the motor using a vibration test rig.

INDEX TERMS Electromagnetic vibration, squirrel-cage induction motor, load condition, electromagnetic force wave.

I. INTRODUCTION

The three-phase squirrel-cage induction motor has been widely used due to its robustness, simple structure, low cost and easy maintenance. In addition, higher demands have been made on the performance of squirrel cage induction motors, such as demands for lower noise and vibration.

The vibration of squirrel-cage induction motors usually includes three categories: mechanical vibration, fluid vibration and electromagnetic vibration [1], [2]. Unlike the mechanical and fluid relevant vibrations, the electromagnetic excitation significantly changes with different loadings and is consequently the main vibration excitation source.

Studies on the main vibration excitation source have been conducted using two main methods: numerical analyses and analytical methods [2]. In numerical analyses, finite element models have been widely used to calculate the transient electromagnetic field, investigate the effect of the magnetic

field saturation on the electromagnetic force, and examine the electromagnetic force distribution [3]–[8].

In analytic methods, the electromagnetic excitation was analyzed by multiplying the magnetomotive force (MMF) by the magnetic permeance [9], and the waves of magnetomotive force and magnetic permeance were obtained by taking the teeth effect and magnetic saturation into consideration [10]. Analytic models were constructed to obtain a suitable magnetic field for different pole slots, radial electromagnetic forces and no-load magnetic fields of motors [11]–[13]. Simple and clear as it is, this method barely considers the effect of the actual mechanical structure of the motor on the vibration. Studies on the vibration under different load conditions have established the correlation between motor vibration and load conditions but failed to associate the vibration with the force waves [14].

A combination of these two methods based on the finite element has been proposed to study air gap magnetic fields and electromagnetic force waves [15], [16]. The actual armature reaction magnetic field of the air gap was determined after combining the excitation effects of all slot currents with

The associate editor coordinating the review of this manuscript and approving it for publication was Xiaodong Sun.

the calculated armature reaction magnetic field when the single slot is energized [17].

On the other hand, the vibrations, noise and electromagnetic force waves of different working conditions were calculated [18].

In addition, the finite element method was utilized to estimate the rotor magnetomotive force; then, the semianalytical subdomain method was adopted to evaluate and optimize the electromagnetic force and vibration performance of the built-in motor [19]–[22].

The frequency characteristics of the motor vibration and noise coincide with the radial electromagnetic force wave, so the radial electromagnetic force wave is considered to be the main cause of motor vibration [23]–[27]. Despite the increasing application of the finite element method, the correlation between the motor vibration and electromagnetic force wave has not been fully studied and verified through practical tests [28].

This paper first determines the spatial and temporal distributions of the radial electromagnetic force using the Maxwell tensor method and then calculates the radial force using the finite element method. The calculated results are decoded through a 2D fast Fourier transform to obtain the amplitude of the electromagnetic force at spatial order under different loads. In addition, by analyzing the electromagnetic vibration under varied load conditions, this study determines the frequency variations of the electromagnetic vibration in the case of nonresonance and identifies the dominant electromagnetic force waves that affect the electromagnetic vibration. Finally, the results are verified using experiment in which the mechanical and electromagnetic vibrations are separated, and the vibration of the stator is tested individually.

II. ANALYSIS OF THE ELECTROMAGNETIC FORCE

When the motor is in operation, the currents of the stator and rotor interact to produce a composite air gap magnetic field, which contains a large number of frequencies and rotating force waves in the spatial distribution. Therefore, the radial electromagnetic force waves can be expressed as [9]

$$p_r(\theta, t) = \sum_n P_n \cos(\omega_n t - n\theta + \phi_n) \tag{1}$$

where p_r is the rth-order radial electromagnetic force wave; P_n is the nth-order force wave amplitude. ω is the angular speed. n and r are the orders ($n = \pm1, \pm2, \dots$); θ is the azimuth angle; t is time; and φ_n is the phase angle.

According to Maxwell stress tensor, the radial magnetic force per unit area or magnetic pressure waveform in the air gap of the stator of the air gap is [9]

$$p_n(\theta, t) = \frac{1}{2\mu_0} \left[B_r^2(\theta, t) - B_t^2(\theta, t) \right] \tag{2}$$

where μ_0 is the permeability of vacuum; B_r and B_t are the radial and tangential components of the magnetic flux density in the air-gap.

In the formula above, since the magnitude of the tangential force wave is small, B_t is neglected in the calculation [29], [30], and the radial magnetic density is expressed as [9]

$$B_r(\theta, t) = f(\theta, t)\lambda(\theta, t) \tag{3}$$

where $f(\theta, t)$ is the air gap magnetomotive force, and $\lambda(\theta, t)$ is the air gap magnetic permeance.

Neglecting the higher orders and constant component of the electromagnetic force, we have

$$
\begin{aligned}
p_n(\theta, t) &= \frac{B_r^2}{2\mu_0} \\
&= \frac{1}{2\mu_0} \left\{ \begin{array}{l} \dfrac{B_1^2}{2} \cos(2p\theta - 2\omega_1 t - 2\phi_{0r}) \\ + \displaystyle\sum_{vz}\sum_{\mu z} \begin{array}{l} B_{vz}B_{\mu z}\cos[(\mu \pm v)\theta - \\ (\omega_\mu \pm \omega_1)t - (\phi_{\mu r} \pm \phi_{vr})] \end{array} \end{array} \right\}
\end{aligned} \tag{4}
$$

where

$$\omega_\mu = k_2 Z_2/p(1-s)\omega_1 + \omega_1 \tag{5}$$

B_1 is the fundamental magnetic flux density, p is the pole pairs, ω_1 is the angular velocity, φ_{0r}, $\varphi_{\mu z}$, and φ_{vz} are the phase angles of different harmonic magnetic fields, B_{vz} is the magnitude of the v_z stator harmonic magnetic field, $B_{\mu z}$ is the magnitude of the μ_z rotor harmonic magnetic field, v is the number of stator harmonics, μ is the number of rotor harmonics, v_z is the number of stator slot harmonics, μ_z is the number of rotor slot harmonics, $v_z = k_1 Z_1 \pm p$, and $\mu_z = k_2 Z_2 \pm p$.

The additional electromagnetic excitation at the presence of k times power harmonics is

$$
p_{nk}(\theta, t) = \frac{1}{2\mu_0} \left\{ \begin{array}{l} \displaystyle\sum F_0 F_k \Lambda_0^2 \cos[(p \pm p)\theta \\ -(\omega_k \pm \omega_1)t - (\phi_k \pm \phi_0)] \\ + \dfrac{1}{2} \displaystyle\sum F_k^2 \Lambda_0^2 \cos(2p\theta - 2\omega_k t - 2\phi_k) \end{array} \right\} \tag{6}
$$

where F_0 is the fundamental MMF, F_k is the MMF of the k time harmonic current, φ_k is the MMF initial phase angle of k times harmonic current, and ω_k is the harmonic angular velocity.

According to the above derivation, the main orders and frequencies of the MMF, magnetic permeability, electromagnetic force waves, and current harmonic are listed in Table 1. Due to the increased temperature under load, these natural frequencies will change slightly when they are measured during normal operation [23].

The natural frequency of the stator of the machine system of the mth circumferential vibrational mode can be simplified as [2]

$$f_m = \frac{1}{2\pi} \sqrt{\frac{K_m}{M_m}} \tag{7}$$

where K_m is the lumped stiffness, and M_m is the lumped mass of the stator system.

TABLE 1. Components of the electromagnetic force waves in the squirrel-cage induction motor.

	type	Order	Frequency
MMF wave	Fundamental wave	p	f
	Phase band harmonic	$(6k\pm1)\,p$	f
	Stator slot harmonics	$k_1Z_1\pm p$	f
	Rotor slot harmonics	$k_2Z_2\pm p$	$[k_2Z_2/p(1\text{-}s)\pm1]f$
	Constant magnetic Permeance waves	0	0
Permeance waves	Stator slot permeance harmonics	k_1Z_1	0
	Rotor slot permeance harmonics	k_2Z_2	$k_2Z_2/p(1\text{-}s)f$
	Product of stator and rotor permeance harmonics	$\pm k_1Z_1\text{-}k_2Z_2$	$k_2Z_2/p(1\text{-}s)f$
	Fundamental wave force	$2p$	$2f$
Force waves	Product of stator and rotor force wave	$\mu_z\pm v_z$	$k_2Z_2/p(1\text{-}s)f+2f$ $k_2Z_2/p(1\text{-}s)f$
	k times harmonic in the power supply	$p\pm p$ $2p$	$f_k\pm f$ $2f_k$

note：　$k_1, k_2, k_3 = \pm1, \pm2, \pm3 \ldots v_z = k_1Z_1\pm p,\ \mu_z = k_2Z_2\pm p$

TABLE 2. Parameters of the motor.

Rate power	7.5 kW	Rate voltage	380 V
Stator slots	36	Rotor slots	28
Pole pairs	2	skewed	0 rad
Air gap length	0.5 mm	Core length	160 mm
Stator diameter	210 mm	Rotor diameter	135 mm

According to the theory of mechanical vibration impedance [2], the amplitude of the vibration displacement of mode m can be derived as

$$A_m = \frac{F_m/M}{\sqrt{\left(\omega_m^2 - \omega_r^2\right)^2 + 4\zeta_m^2\omega_r^2\omega_m^2}} \qquad (8)$$

where M is the mass of the cylindrical shell, ω_n is the angular natural frequency of mode m, ω_r is the angular frequency of the force component of order r, ζ_m is the modal damping ratio, and F_m is the amplitude of exciting force.

When the squirrel-cage induction motor is operated with a load, its speed decreases, and the slip rate increases, which changes the electromagnetic force wave. The relationship between the frequency and the motor slip rate is

$$\Delta f = k\frac{f_1Z_2}{p}s \qquad (9)$$

where f_1 is the power frequency, Z_2 is the rotor slot, s is the slip, and p is the pole-pairs, $k = 1, 2, 3 \ldots$.

This paper calculates the excitation amplitude of the harmonics for 5 operating conditions: without load and 25%, 50%, 75%, and 100% rated load. By comparing the calculated amplitude with vibration, we obtain the vibration increase caused by the load. The 0th-order and 4th-order magnitudes of the forces under different loads are presented in Table 3.

Table 3 indicates that the vibration caused by the excitation force wave is related to the amplitude and the order of the force wave. For the small motor, the lower order of the force wave corresponds to the larger vibration [2]. For example, the 0th-order and the 4th-order force waves have great impact on the motor vibration (the electromagnetic forces of the 8th-order and above are neglected due to their minor impact). For a motor of 2 pole pairs, the 4th-order 100 Hz electromagnetic force is substantially larger than the forces of other orders. However, due to its symmetric distribution and the large radial stiffness of small motors, the 4th-order electromagnetic force imposes a small impact on the vibration. Among the electromagnetic forces generated by the interaction of the stator and rotor harmonics, the 1st-order forward rotor slot harmonic and reverse stator slot harmonic of the 4th-order electromagnetic force produce a considerable electromagnetic force, whose amplitude reaches 6927 Pa (100% load). Although amplitudes much lower than this are caused by the interaction of the 1st-order rotor-stator slot harmonics, the electromagnetic force amplitude produced by other harmonics increases when the motor is loaded. The calculation of electromagnetic excitation suggests that the amplitude of the low-order electromagnetic force generally increases with increase in loading, but the natural frequency of motor slightly changes. As a result, the vibration amplitude of the motor increases.

Instead of calculating the vibration response of the motor, this study calculates the electromagnetic force wave to

TABLE 3. Frequency and amplitude of the em force wave under different loads.

	no-load		25% load		50% load		75% load		100% load	
Order	Freq (Hz)	Amp (Pa)	Freq (Hz)	Amp (Pa)	Freq (Hz)	Amp (Pa)	Freq (Hz)	Amp (Pa)	Freq (Hz)	Amp (Pa)
0	600	82	598	157	597	326	593	624	582	1160
0	1499	10	1496	15	1493	29	1485	54	1464	100
0	2099	17	2094	23	2090	38	2078	66	2045	121
0	2698	69	2693	82	2687	169	2670	290	2627	439
0	3598	155	3591	175	3584	219	3563	324	3509	463
4	100	121037	100	121037	100	121037	100	121908	100	121908
4	700	75	698	139	697	285	693	543	682	1007
4	700	42	698	81	697	167	693	320	682	595
4	800	740	798	1315	797	2429	793	4359	782	6927
4	1299	12	1296	19	1293	36	1285	67	1264	125
4	1399	11	1396	16	1393	31	1385	58	1364	107
4	1399	22	1396	33	1393	62	1385	116	1364	216
4	2798	69	2793	81	2787	165	2770	281	2727	425
4	2798	228	2793	261	2787	352	2770	560	2727	803
4	2898	11	2893	13	2887	19	2870	33	2827	59
4	3398	10	3391	12	3384	16	3363	26	3309	47
4	3498	155	3491	176	3484	222	3463	331	3409	475
4	3498	33	3491	41	3484	97	3463	160	3409	257
4	5496	29	5485	33	5474	44	5440	64	5354	116

Note: Freq is the frequency, and Amp is the amplitude.

TABLE 4. Vibration mode and natural frequency of the stator.

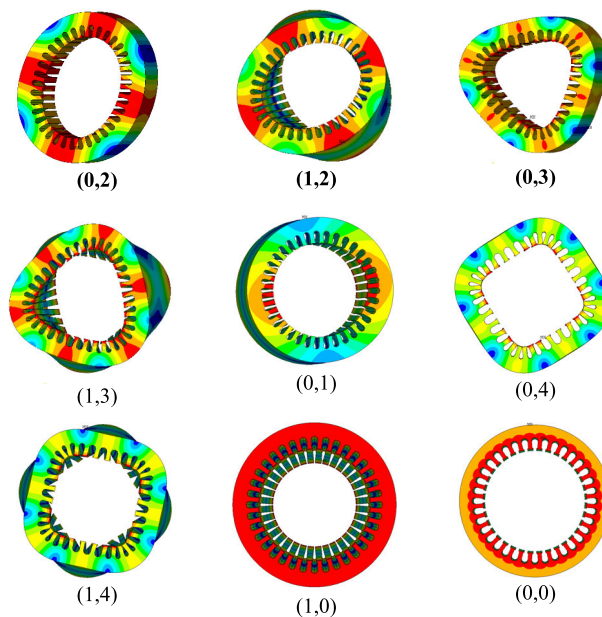| Vibration order	Frequency/Hz
(0,2)	1155.2
(1,2)	1665.5
(0,3)	3087.3
(1,3)	3853.4
(0,1)	5470.1
(0,4)	5515.9
(1,4)	6311.6
(1,0)	6772.2
(0,0)	6909.1
(2,2)	7533.5
(2,2)	7636.1

FIGURE 1. Modes of the stator core obtained by the FE simulation.

estimate the vibration variation of the motor under different working conditions.

III. MODAL ANALYSIS OF THE STATOR CORE
A modal analysis is performed using the finite element simulation. The number of nodes is 1,036,213, and the number of elements is 41,188. The vibration modes of the core are shown in Figure 1. Table 4 shows the modal analysis results, including the frequency and mode shape of the core.

IV. SIMULATION RESULT
To better explain the electromagnetic vibration characteristics of the motor under different loads, the finite element software is utilized to calculate the magnetic flux density of the air gap to determine the density distribution of the electromagnetic excitation force.

Figure 2 show the topologies of the motor model with the air gap centerline. As shown, the mesh number of elements in the squirrel-cage induction motor with different loads is 61161. The 100% load torque is 47.5 Nm.
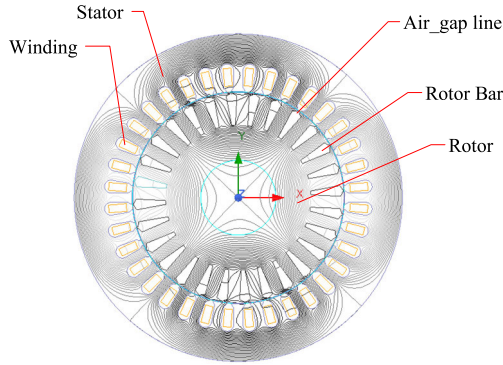
FIGURE 2. Cross section with the magnetic flux lines of the motor model.
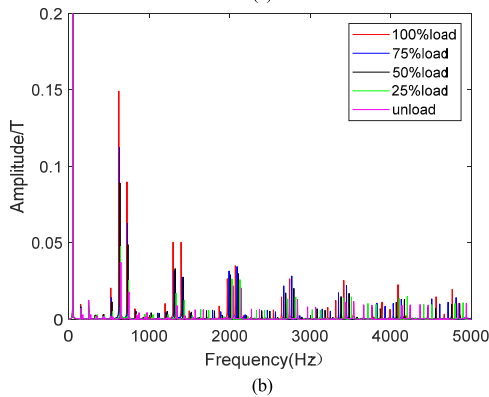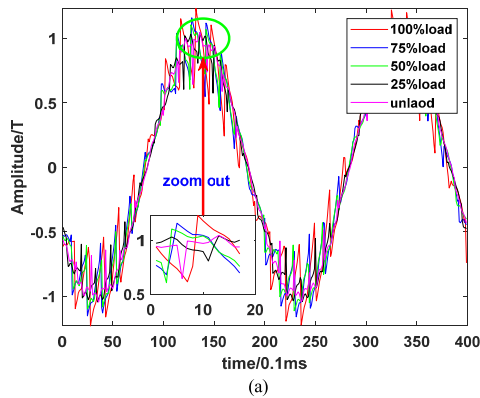

FIGURE 3. Time magnetic flux density of the air gap under difference loads: (a) time domain; (b) frequency domain.

Figure 3a shows the radial magnetic flux density of a certain point on the X axis of the air gap central line between the stator and rotor with different loads. The variation trend of the air gap magnetic density in the time domain is not easy to observe, so it is transferred to the frequency domain.

Fourier transform is performed on the load time domain magnetic flux density to determine the magnetic flux density frequency amplitude, as shown in Figure 3b. When the load increases, the amplitude of the harmonic field increases; the 1st- and 2nd-order rotor slot harmonics have the most significant increases, while the frequency decreases. When the rotor bar current increases with the increasing load, the rotor magnetic field in the circuit gains strength. As a result, the rotor slot harmonics become larger.
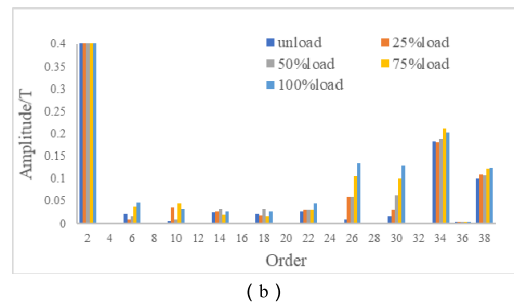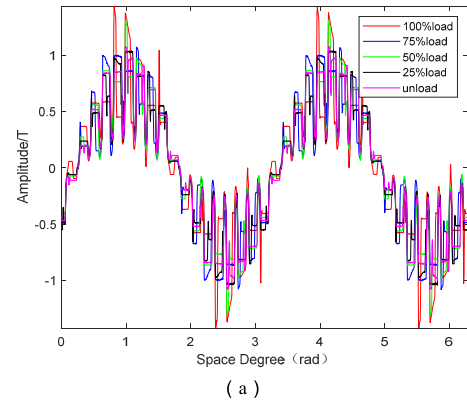

FIGURE 4. Spatial radial magnetic flux density of the air gap under different loads (a) space; (b) spatial order.

Figure 4a shows the change in radial magnetic density on a circular path within the air gap at a certain time when the load varies. Apparently, the air gap portion between the stator slot and the rotor has a large magnetic flux density, while the air gap portion between stator slots has a magnetic flux density of almost zero. Due to the difference in air gap clearance, the magnetic resistance changes, which causes a remarkable amplitude fluctuation of the magnetic density. When the load increases, the amplitude of the fundamental wave for the air gap radial magnetic density significantly increases, and the harmonics become more pronounced.

A main order diagram (Figure 4b) is obtained by performing Fourier transform on the spatial air gap magnetic density of different load conditions. In the diagram, the spatial fundamental frequency is the reciprocal of the mechanical circumferential angle. As demonstrated in the diagram, the order for the fundamental wave of the 4-pole motor is 2, and the fundamental wave barely changes. However, $Z_2 \pm p$ (the 26th-order and 30th-order force wave) changes most significantly and is the first-order slot harmonic of the rotor magnetic potential. $Z_1 \pm p$ (the 34th- and 38th-order force wave) also displays a noticeable change and is the first-order slot harmonics of the stator magnetic potential. When the motor is running with a load, the increased current causes a large increase in amplitude of the magnetic flux density of the stator and rotor.

The temporal and spatial comparison of the air gap magnetic flux density shows that there is no clear trend in the variation of the magnetic density amplitude of each order under different load conditions. The data in Table 5 show

TABLE 5. Flux indensity of the main harmonic order under different loads unit: tesla.

spatial order	no-load	25% load	50% load	75% load	100% load	growth rate (%)
2	0.782	0.773	0.766	0.757	0.745	-4.7%
6	0.021	0.010	0.015	0.038	0.046	121%
10	0.007	0.037	0.010	0.044	0.033	394%
14	0.025	0.027	0.032	0.018	0.028	9.5%
18	0.020	0.017	0.032	0.016	0.027	33.3%
22	0.026	0.031	0.030	0.030	0.044	66.5%
26	0.010	0.040	0.060	0.105	0.135	1223%
30	0.015	0.030	0.062	0.100	0.128	753%
34	0.184	0.182	0.188	0.213	0.203	10%
38	0.099	0.109	0.108	0.123	0.125	26%
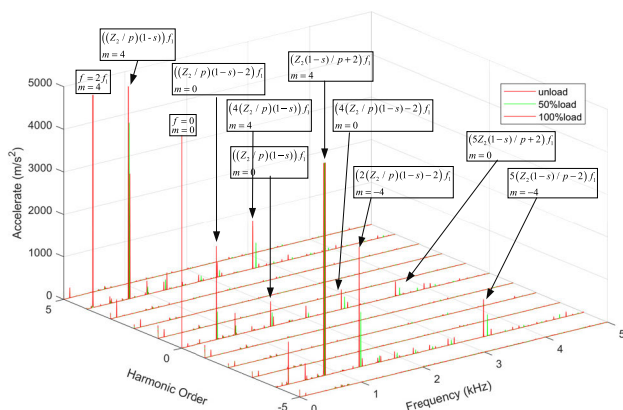
FIGURE 5. Electromagnetic force wave under different loads.

FIGURE 6. Testing system.

that the 26th-order rotor slot harmonic increases most significantly, and the magnetic flux density of this order increases by 12 times from no-load to 100% of the rated load. Therefore, the 26th-order rotor slot harmonic is most affected by load the most.

The separate analyses of the temporal and spatial changes of the magnetic flux density are shown above. To analyze the changes in these two dimensions together, the electromagnetic force wave generated by the air gap magnetic density is calculated. The harmonics of the radial electromagnetic force are analyzed using 2D fast Fourier transform (2D-FFT) under different load conditions. 2D-FFT is performed on the air gap magnetic density, and a three-dimensional diagram of the electromagnetic force wave is obtained with respect to the frequency, order and amplitude. For a clear comparison, only three conditions of no-load, 50% load and 100% load are selected. As shown in Figure 5, almost identical to the change in air gap magnetic flux density, the electromagnetic force amplitude increases when the load increases. When the motor is running with a load, more frequencies of the electromagnetic force are produced, and the amplitude greatly increases. When the frequency of the force wave does not coincide with the natural vibration frequency of the stator core, the amplitude of the vibration increases when the load increases.
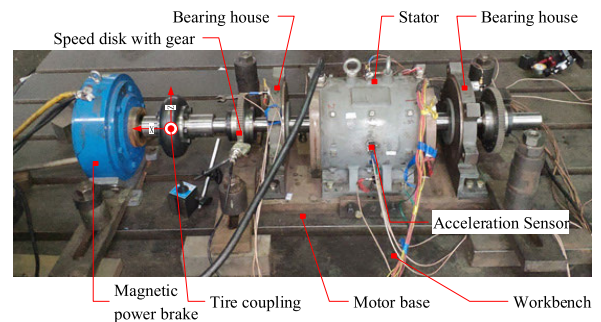
V. EXPERIMENTAL VERIFICATION
A. DESIGN OF THE TEST RIG
A test rig is designed to separate the electromagnetic excitation from the mechanical excitation of the motor under various operating conditions. To this end, the bearing housing and stator were separately mounted on a base plant of large rigidity. Meanwhile, the cooling fan was disassembled to minimize the fluid noise. To ensure the concentricity of the end cover and casing structure, the components were machined with higher precision, and the bearing housing was installed with a dial gauge. A feeler gauge was used to measure the air gap clearance.

The test rig design is shown in Figure 6.

The measuring points are shown in Figure 5. In the load test, a magnetic powder brake served as the load with magnetic powder as the working medium. The magnetic powder on the brake disc was controlled by adjusting the supply current to generate the resistance torque, which had a good linear relationship with the supply current. Connected by a coupling, the motor and magnetic powder brake were fixed on the cast iron bench.

In Figure 7, X, Y and Z indicate the axial, lateral and vertical directions, respectively. The acceleration sensors were placed at points P1-P7, which were the no-load end bearing housing, motor base top, motor foot, base plate beneath the motor base, bearing housing, bearing housing foot, and the top of the magnetic power brake in sequence.
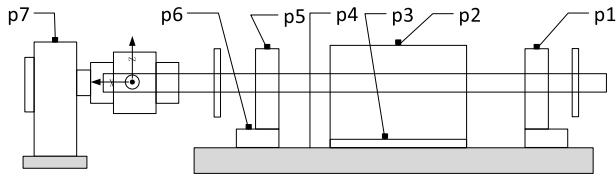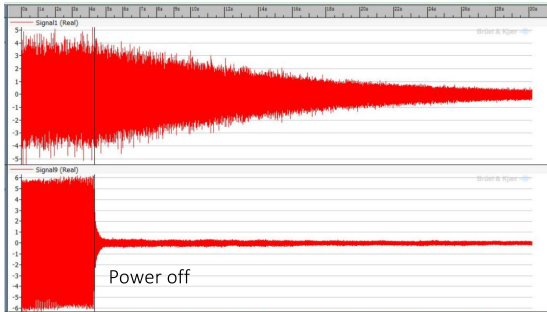
FIGURE 7. Measuring point diagram.

FIGURE 8. Acceleration of P1Y and P2Y in the time domain when the power is cut off.

FIGURE 9. Vibration in elastic pin coupling connection under different loads.
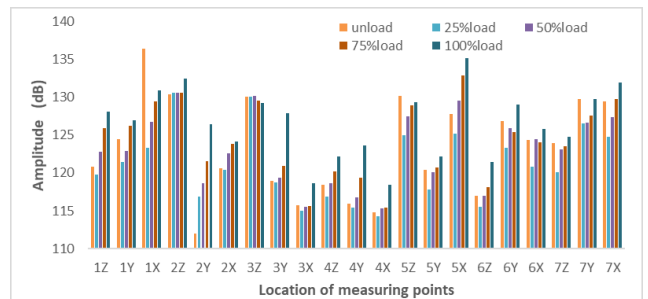
FIGURE 10. Vibration in tire coupling connection under different loads.

B. VERIFICATION OF THE TEST

When the motor that was running without a load had a sudden power cut, the electromagnetic excitation instantly disappeared, but the rotor excitation remained due to inertia. The time domain diagram of acceleration at testing points P1 and P2 at the moment of power off was obtained, as shown in Figure 8. The diagram illustrates that the stator acceleration response immediately disappears after the power turns off, while the rotor vibration response gradually decreased. Because the electromagnetic vibration will disappear when the power is off, it can be concluded that the stator mainly has electromagnetic vibration. Therefore, it can be verified that the bench managed to separate the electromagnetic excitation from the mechanical excitation.

C. TESTING

In the loaded test, the load torque was adjusted by changing the current of the controller. After the torque calibration with a torque sensor, the data were collected for five working conditions, namely, no-load, 25% load, 50% load, 75% load and 100% load, in two modes of elastic pin coupling connection and tire coupling connection. The data are shown in Figure 8 and Figure 9.

In Figures 9 and 10, the vibration amplitudes of the testing points gradually increase when the load grows, and the vibration amplitude of the motor connected to the load by the tire coupling is smaller than that connected by the elastic pin coupling.

D. DISCUSSION

This study focuses on the motor electromagnetic vibration and analyzes the vibration spectrum of testing points P2 and
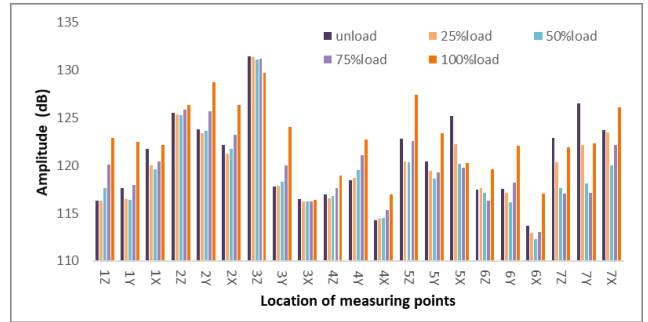

FIGURE 11. Amplitude of the vibration acceleration under different loads.
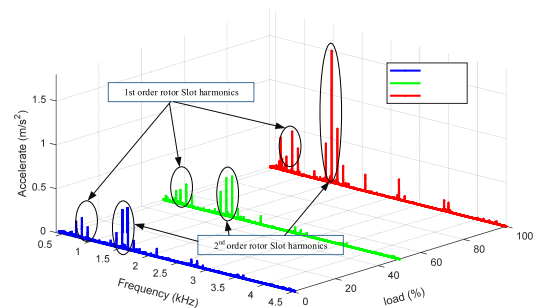
P3 under different loads when the motor and load are connected by the elastic pin coupling.

The vibration trend under various load conditions is consistent with the simulated magnetic density and electromagnetic force wave, and the vibration of the slot harmonics shows distinct characteristics. The test magnetic density spectrum displays the ±1-, ±2-, ±3- and other-order rotor slot harmonic magnetic densities, which are $Z_2/p(1-s)f_1$, $Z_2/p((1-s)-2)f_1$, $2Z_2/p((1-s)-2)f_1$, $3Z_2/p((1-s)-2)f_1$, etc.

In addition, the low-frequency vibration is clearly significant in the no-load condition. Figure 11 shows that when the load increases, the amplitude of the harmonic magnetic field increases, whereas the amplitude of the fundamental wave barely changes. However, the 1st-order rotor slot harmonics displays the largest growth. When the load increases, the frequency decreases because of the increasing slip rate and lower rotation speed.

VI. CONCLUSION

This paper analyzes the influence of the electromagnetic excitation force on the electromagnetic vibration of a motor under different load conditions and verifies the simulation results by testing the electromagnetic vibration under different working conditions on the motor vibration separation test bench. The following conclusions are made:

(1) When the motor is running with a load, the harmonic magnetic field of the air gap slot greatly increases. Most of the response frequencies come from electromagnetic force waves generated by the interaction between stator and rotor slot harmonics.

When the motor runs without a load, the main vibration of the motor is concentrated in the low-frequency band. When the motor operates under a load condition, the high-frequency vibration of the motor greatly increases, and the main frequency feature is the harmonic frequency of the rotor slot.

(2) After the motor has been loaded, due to the larger current, the amplitude of the interaction force of the stator and rotor increase, which result in significant vibration of different parts of the whole machine.

(3) After the motor is loaded, the rotor and stator slot harmonics in the first order and second order demonstrate the largest change, which is the major cause for the difference between the no-load and load vibration response.

(4) The results of the vibration test suggest that the coupling stiffness can affect the vibration amplitude, and the smaller rigidity of the coupling can reduce the amplitude of the motor vibration.

(5) The relationship between the electromagnetic force wave and the motor magnetic vibration was theoretically shown. The effect of electromagnetic vibrations under the loading was experimentally discussed. It has been clarified that the dominant electromagnetic vibration increases in approximate proportion to the amplitude of the low-order harmonic, which is the main cause of the vibration.

DATA AVAILABILITY

The data used to support the findings of this study are available from the corresponding author upon request.

CONFLICTS OF INTEREST

The authors declare no conflicts of interest.

REFERENCES

[1] S. J. Yang, *Low-Noise Electrical Motors*. Oxford, U.K.: Clarendon, 1981.

[2] J. F. Gieras, C. Wang, and J. C. Lai. *Noise of Polyphase Electric Motors*. New York, NY, USA: Taylor & Francis, 2006, pp. 5–19.

[3] A. Belahcen, A. Arkkio, P. Klinge, J. Linjama, V. Voutilainen, and J. Westerlund, "Radial forces calculation in a synchronous generator for noise analysis," in *Proc. 3rd Chin. Int. Conf. Elect. Mach.*, Xi'an, China, Aug. 1999, pp. 122–199.

[4] P. J. Rodriguez, A. Belahcen, and A. Arkkio, "Signatures of electrical faults in the force distribution and vibration pattern of induction motors," *IEE Proc.—Electric Power Appl.*, vol. 153, no. 4, pp. 523–529, Jul. 2006.

[5] T. P. Holopainen, A. Tenhunen, and A. Arkkio, "Electromechanical interaction in rotordynamics of cage induction motors," *J. Sound Vib.*, vol. 284, nos. 3–5, pp. 733–755 2005.

[6] M. Valavi, A. Nysveen, and R. Nilssen, "Characterization of radial magnetic forces in low-speed permanent magnet wind generator with non-overlapping concentrated windings," in *Proc. 20th Int. Conf. Elect. Mach. (ICEM)*, Sep. 2012, pp. 2943–2948.

[7] X. Sun, Z. Shi, G. Lei, Y. Guo, and J. Zhu, "Analysis and design optimization of a permanent magnet synchronous motor for a campus patrol electric vehicle," *IEEE Trans. Veh. Technol.*, vol. 68, no. 11, pp. 10535–10544, Nov. 2019, doi: 10.1109/TVT.2019.2939794.

[8] X. Sun, K. Diao, G. Lei, Y. Guo, and J. Zhu, "Study on segmented-rotor switched reluctance motors with different rotor pole numbers for BSG system of hybrid electric vehicles," *IEEE Trans. Veh. Technol.*, vol. 68, no. 6, pp. 5537–5547, Jun. 2019, doi: 10.1109/TVT.2019.2913279.

[9] Y. X. Chen, Z. Q. Zhu, and S. C. Ying, *Analysis and Control of Motor Noise*. Hangzhou, China: Zhejiang Univ. Press, 1987.

[10] S. P. Verma and A. Balan, "Determination of radial-forces in relation to noise and vibration problems of squirrel-cage induction motors," *IEEE Trans. Energy Convers.*, vol. 9, no. 2, pp. 404–412, Jun. 1994.

[11] L. J. Wu, Z. Q. Zhu, D. Staton, M. Popescu, and D. Hawkins, "Subdomain model for predicting armature reaction field of surface-mounted permanent-magnet machines accounting for tooth-tips," *IEEE Trans. Magn.*, vol. 47, no. 4, pp. 812–822, Apr. 2011.

[12] H. Guhuan, Z. Huang, and D. Chen, "Two-dimensional field analysis on electromagnetic vibration-and-noise sources in permanent-magnet direct current commutator motors," *IEEE Trans. Magn.*, vol. 47, no. 4, pp. 787–794, Apr. 2011.

[13] J. Fu and C. Zhu, "Subdomain model for predicting magnetic field in slotted surface mounted permanent-magnet machines with rotor eccentricity," *IEEE Trans. Magn.*, vol. 48, no. 5, pp. 1906–1917, May 2012.

[14] K. Tsuboi, I. Hirotsuka, and F. Ishibashi, "Causes and characteristics of the electromagnetic vibration of a squirrel cage induction motor under load," *Electr. Eng. Jpn.*, vol. 120, no. 4, pp. 81–89, 2015.

[15] X. Sun, B. Su, S. Wang, Z. Yang, G. Lei, J. Zhu, and Y. Guo, "Performance analysis of suspension force and torque in an IBPMSM With V-shaped PMs for flywheel batteries," *IEEE Trans. Magn.*, vol. 54, no. 11, Nov. 2018, Art. no. 8105504.

[16] X. Sun, Z. Jin, S. Wang, Z. Yang, K. Li, Y. Fan, and L. Chen, "Performance improvement of torque and suspension force for a novel five-phase BFSPM machine for flywheel energy storage systems," *IEEE Trans. Appl. Supercond.*, vol. 29, no. 2, pp. 1–5, Mar. 2019, Art. no. 0601505.

[17] W. Zhu, B. Fahimi, and S. Pekarek, "A field reconstruction method for optimal excitation of permanent magnet synchronous machines," *IEEE Trans. Energy Convers.*, vol. 21, no. 2, pp. 305–313, Jun. 2006.

[18] D. Torregrossa, A. Khoobroo, and B. Fahimi, "Prediction of acoustic noise and torque pulsation in PM synchronous machines with static eccentricity and partial demagnetization using field reconstruction method," *IEEE Trans. Ind. Electron.*, vol. 59, no. 2, pp. 934–944, Feb. 2012.

[19] E. Devillers, M. Hecquet, E. Devillers, and J. Le Besnerais, "A new hybrid method for the fast computation of airgap flux and magnetic forces in IPMSM," in *Proc. 12th Int. Conf. Ecolog. Vehicles Renew. Energies (EVER)*, Apr. 2017, pp. 1–8.

[20] W. Xun and Q. Arui, "Analytical calculation for harmonics in squirrel-cage asynchronous motors considering slotting and saturation," *J. Tsinghua Univ. (Sci. Tech.)*, vol. 51, no. 3, pp. 18–28, 2011.

[21] H. Yang and Y. Chen, "Influence of radial force harmonics with low mode number on electromagnetic vibration of PMSM," *IEEE Trans. Energy Convers.*, vol. 29, no. 1, pp. 38–45, Mar. 2014.

[22] Y. Lu, J. Li, R. Qu, D. Ye, and H. Lu, "Electromagnetic force and vibration study on axial flux permanent magnet synchronous machines with dual three-phase windings," *IEEE Trans. Ind. Electron.*, vol. 67, no. 1, pp. 115–125, Jan. 2020, doi: 10.1109/TIE.2018.2890494.

[23] J. Zou, H. Lan, Y. Xu, and B. Zhao, "Analysis of global and local force harmonics and their effects on vibration in permanent magnet synchronous machines," *IEEE Trans. Energy Convers.*, vol. 32, no. 4, pp. 1523–1532, Dec. 2017, doi: 10.1109/TEC.2017.2720422.

[24] S. Yu and R. Tang, "Electromagnetic and mechanical characterizations of noise and vibration in permanent magnet synchronous machines," *IEEE Trans. Magn.*, vol. 42, no. 4, pp. 1335–1338, Apr. 2006.

[25] S.-W. Hwang, H.-J. Lee, T.-S. Kim, Y.-H. Jung, and J.-P. Hong, "The influence of electromagnetic force upon the noise of an IPM motor used in a compressor," *IEEE Trans. Magn.*, vol. 42, no. 10, pp. 3494–3496, Oct. 2006.

[26] K. H. Yim, J. W. Jang, G. H. Jang, M. G. Kim, and K. N. Kim, "Forced vibration analysis of an IPM motor for electrical vehicles due to magnetic force," *IEEE Trans. Magn.*, vol. 48, no. 11, pp. 2981–2984, Nov. 2012.

[27] H. J. Shin, J. Y. Choi, H. W. Cho, and K. Hong, "Effects of mechanical resonance on vibrations of mechanical systems with permanent magnet machines," *IEEE Trans. Magn.*, vol. 50, no. 11, pp. 1–4, Nov. 2014.

[28] D. Fodorean, M. M. Sarrazin, C. S. Marţiş, J. Anthonis, and H. Van der Auweraer, "Electromagnetic and structural analysis for a surface-mounted PMSM used for light-EV," *IEEE Trans. Ind. Appl.*, vol. 52, no. 4, pp. 2892–2899, Jul./Aug. 2016.

[29] D. G. Dorrell, "Sources and characteristics of unbalanced magnetic pull in three-phase cage induction motors with axial-varying rotor eccentricity," *IEEE Trans. Ind. Appl.*, vol. 47, no. 1, pp. 12–24, Feb. 2011.

[30] D. G. Dorrell, J. K. H. Shek, M. A. Mueller, and M.-F. Hsieh, "Damper windings in induction machines for reduction of unbalanced magnetic pull and bearing wear," *IEEE Trans. Ind. Appl.*, vol. 49, no. 5, pp. 2206–2216, Sep. 2013.
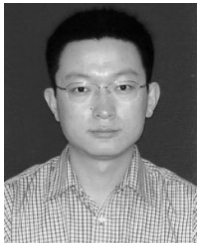
WANYOU LI received the B.Sc., M.Sc., and Ph.D. degrees in marine engineering from Harbin Engineering University, Heilongjiang, China, in 1995, 1998, and 2002, respectively.

His main research interest includes the structure vibration control of rotating machinery of electromechanical equipment.

DEFENG KONG received the B.Sc. and M.Sc. degrees in agricultural mechanization engineering from Heilongjiang Bayi Agricultural University, Daqing, China, in 2003 and 2007, respectively. He is currently pursuing the Ph.D. degree with the College of Power and Energy Engineering, Harbin Engineering University, Harbin, China.

His current research interests are the analysis of electromagnetic field and vibration control of electrical machines.

ZHIJUN SHUAI received the B.Sc., M.Sc., and Ph.D. degrees in marine engineering from Harbin Engineering University, Heilongjiang, China, in 2002, 2006, and 2013, respectively.

He has been working with Harbin Engineering University, since 2013, where he is currently an Associate Professor with the College of Power and Energy. Since 2006, he has been engaging in the research of vibration and noise reduction, load identification, and structural dynamics optimization of marine motors. His research interests include the structure vibration control of rotating machinery and analysis of the electromagnetic field of electrical machines.

DONGHUA WANG received the B.Sc. degree in thermal power engineering and the M.Sc. and Ph.D. degrees in power machinery and engineering from the Harbin Institute of Technology, Heilongjiang, China, in 2002, 2004, and 2009, respectively.

He has been working with Harbin Engineering University, since 2009, where he is currently an Associate Professor with the College of Power and Energy. His main research interests include the dynamics of rotating machinery and structure vibration control.

• • •